POLITECNICO
MILANO 1863

DIPARTIMENTO DI MECCANICA

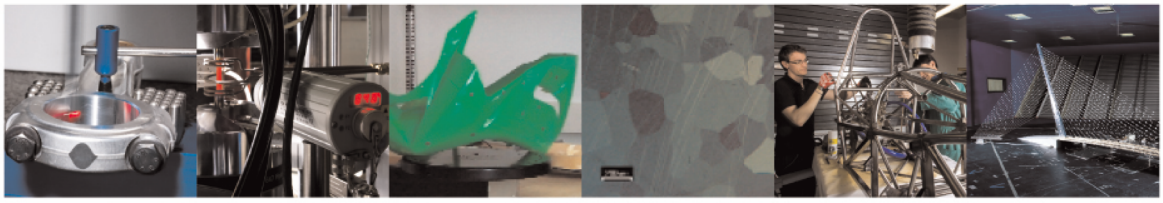

On the mitigation of the RAPID algorithm uneven sensing network issue employing averaging and Gaussian blur filtering techniques

GONZÁLEZ JIMÉNEZ Á.;Lomazzi L.;Cadini F.;Beligni A.;Sbarufatti C.;Giglio M.;Manes A.

This is a post-peer-review, pre-copyedit version of Alvaro Gonzalez-Jimenez, Luca Lomazzi, Francesco Cadini, Alessio Beligni, Claudio Sbarufatti, Marco Giglio, Andrea Manes,
On the mitigation of the RAPID algorithm uneven sensing network issue employing averaging and Gaussian blur filtering techniques, Composite Structures, Volume 278, 2021, 114716,
ISSN 0263-8223,
https://doi.org/10.1016/j.compstruct.2021.114716

DIPARTIMENTO DI MECCANICA ■ POLITECNICO DI MILANO
via G. La Masa, 1 ■ 20156 Milano ■ EMAIL (PEC): pecmecc@cert.polimi.it
http://www.mecc.polimi.it
Rev. 0

On the mitigation of the RAPID algorithm uneven sensing network issue employing averaging and Gaussian blur filtering techniques.

Alvaro Gonzalez-Jimenez, Luca Lomazzi, Francesco Cadini, Alessio Beligni, Claudio Sbarufatti, Marco Giglio, Andrea Manes*

Politecnico di Milano, Department of Mechanical Engineering, via la Masa, 1, 20156, Milan, Italy

Corresponding author: andrea.manes@polimi.it

Abstract

Ultrasonic guided waves-based Structural Health Monitoring (SHM) is a promising solution to perform damage diagnosis in plate-like structures. In this field, the Reconstruction Algorithm for Probabilistic Inspection (RAPID) is one of the most widely used tomographic algorithms to perform active damage detection and localisation. Even though this algorithm is easily implementable, very versatile and satisfactorily accurate, it presents some disadvantages, such as the production of artefacts determined by non-uniform distributions of the sensing network density. In the present article, a processing and spatial filtering technique is proposed, which strongly mitigates the aforementioned problem. The proposed methodology is validated using a numerical database created for a large carbon fibre reinforced polymer (CFRP) with a through-the-thickness hole.

Keywords: SHM; RAPID; composite; Lamb Waves.

1 Introduction

The extensive use of composite materials in the last decades has propelled the advancements in the aeronautical field to a very high degree. However, this usage has posed several new challenges when it comes to the reliability of the mechanical design. In fact, due to the heterogeneous and

laminate nature of composite materials, engineers have faced new failure mechanisms different from the long-studied failure processes of traditional materials. Therefore, the aeronautical sector is in continuous need of tools that allow preventing or, at least, mitigating the extent of the consequences generated by failure in composite-made components.

Improved knowledge of the failure processes of composite materials would have a positive effect on the expense that airlines dedicate to maintenance and repair. For instance, the practical importance of this factor can be appreciated if one observes the cost that civil airlines have dedicated to maintenance and repair [1] in the last years, which drives a revision of the maintenance processes. One of the most promising solutions is the change from a scheduled maintenance program to a more cost-efficient condition-based one [2]. The latter implies that corrective actions will be adopted only when strictly needed or, in other words, when potentially dangerous damage is identified. Hence, a Structural Health Monitoring (SHM) approach of the structure has to be properly set up, to identify eventual deviations from the expected healthy behaviour of the system. This approach relies on the information gathered from a network of sensors permanently installed on the structure, which allows taking measurements on the system that will be later subjected to a post-processing phase to diagnose possible damage scenarios. Within this context, signal post-processing plays a crucial role in damage identification. Hence, the selection and proper implementation of such post-processing algorithms are some of the most crucial parts during the design of an SHM system.

Among all the possible physical phenomena that may be exploited for localising eventual damages, the use of ultrasonic guided waves offers a suitable solution for plate-like structures made of metal and composite materials. Particularly, Lamb waves (LWs) are elastic guided waves that present several interesting features in the damage characterisation field, such as long-distance propagation, even in materials with high attenuation, and high sensitivity to a large variety of defects, even on a small scale [3]. However, they also present a series of drawbacks that should be properly understood for their correct employment. For instance, one of the most critical disadvantages which comes with using LWs is caused by the dispersive behaviour both with the

wave frequency and, considering composite materials, with the fibre orientation [4]–[6]. Additionally, Lamb Waves can propagate according to several modes, which are typically categorised as symmetric (S) and anti-symmetric (A). The fundamental modes, i.e., those characterised by the lowest frequency values, which are labelled S_0 and A_0, are commonly preferred in SHM applications over higher-order modes, since the inherent low frequencies allow limiting the dispersive behaviour of the guided wave [7].

In this context, numerical simulations provide a cost-efficient yet sufficiently accurate solution for studying LWs propagation in composite structures. Several numerical methods exist that allow simulating and analysing Lamb Waves [8]. In particular, the finite element (FE) method and the final difference (FD) method are currently two of the most widely available and easy-to-use simulation methods ([8], [9]). However, for the proper employment of the FE method, some important features, such as mesh dimension, sensor modelling [10] and time step definition [8] should be carefully selected. Maio et al. [4] compared several numerical model formulations based on the overall strategies of the equivalent single-layer approach (ESL) and on the 3D stacked solid layers. They implemented several numerical models to simulate and analyse the dispersive behaviour of LWs in a unidirectional carbon fibre reinforced polymer (CFRP), concluding that the methods based on the equivalent single-layer approach (ESL) provide the most satisfactory trade-off between accuracy of the results and computational cost. Even though ESL-based models do not consider the interlaminar behaviour of composite materials, thus preventing the study of propagation disturbances due to delamination, they are highly advised when dealing with large structures. For this kind of structures, an adequate mesh dimension to guarantee convergence may lead to an extremely large number of nodes in case stacked solid models are considered, thus substantially increasing the computational cost of the simulations.

The Lamb Waves signals gathered either numerically or experimentally from the network of sensors installed on the system, must then be post-processed to identify behaviour that diverge from the healthy baseline. Accordingly, some reconstruction algorithms must be employed for analysing LWs, which allow diagnosing eventual damages within the monitored area. Among the

available reconstruction methods, which rely on consolidated tomographic algorithms already involved in applications different from SHM ([11], [12]), the *Reconstruction Algorithm for Probabilistic Inspection* (RAPID) algorithm is a promising tool for damage detection and localisation [13]. This algorithm commonly requires that a healthy baseline is acquired in the absence of any damage at the early life of the structure, which is stored and later compared to the subsequently acquired data during the operational life of the system. At each interrogation, some damage indexes are computed as a function of the healthy baseline and the currently acquired data, thus allowing the detection of eventual damage and the identification of the corresponding most likely position within the monitored area. Then, a tomography of the structure can be properly built, further processing the algorithm output, which consists of a matrix whose components are the damage probabilities for each of the pixels of interest in the structure. These pixels come from the geometrical discretisation of the monitored area, which has to be set as input to the RAPID method and that will form the tomographic image indicating the damage localisation probabilities. It is worth mentioning that several authors have proposed the implementation of the RAPID algorithm without the need for a baseline comparison [14]–[17]. However, the implementation complexity sharply grows requiring, in most cases, an a priori and complete knowledge of the LWs propagation physics. This fact is accentuated by the anisotropy of composite materials limiting the applicability of these techniques. A baseline comparison method is thus usually preferred for composites.

Notwithstanding the easy implementation and straightforward interpretation of the RAPID algorithm [12], it also presents some weaknesses that, in the authors' opinion, have not been deeply considered in the literature. Liu et al. [18] partially addressed the so-called uneven sensing network density by subtracting a “compensating image”, which identifies the probability distribution tomography when the sensing paths have the same weights. Although there was no appreciable performance improvement in terms of damage localisation between the compensating and standard method, the authors managed to satisfactorily increase the tomography resolution, reducing the extent of the estimated high probability area. However, this method introduces a

subjective user-defined parameter, consisting in a constant weight for the setup of the compensating image. Azuara et al. in [19] also proposed a variation on the RAPID algorithm for solving the uneven density of sensing network. The authors called the modified algorithm RAPID-G. They employed a shape function to diminish the probability around the sensing path intersection points. The final tomography was greatly improved in terms of both contrast and accuracy. Yet, the proposed technique also introduced an extra subjective parameter to define the area of influence of the shape function. Consequently, even if the aforementioned solution provides satisfactory results, it also adds some input parameters, which may decrease the objectivity of the algorithm.

In this paper, a methodology will be presented for solving the uneven sensing network density problem of the RAPID algorithm. The proposed methodology aims at reducing and, possibly, eliminating the artificial high damage probability values determined by the placement of the specific sensors through a two-step approach. First, the paths joining each pair of sensors are determined and the total number of intersections at each pixel of interest of the monitoring area is computed, to define a mitigating action to diminish the artificial contrast between pixels with more intersections and pixels with fewer of them. Moreover, a Gaussian blur filter is further applied to the RAPID algorithm output to construct tomographies with less sharp damage probability peaks coming from the artefacts introduced by the reconstructing algorithm. The algorithm performance will be validated using a numerical FE database for a CFRP panel with a through-hole damage type. Three configurations of sensors will be tested, namely *star*, *circular* and *rectangular*. Additionally, two through-hole diameters, i.e., 5mm and 10mm, and two different positions will be considered for each array of sensors. The present work is intended to be dual-purposed, in that (i) a detailed discussion of the pros and cons of adopting the RAPID algorithm as the tomographic method is given and (ii) a partial solution to the particular problem of uneven sensing network density is presented.

2 RAPID algorithm

The theory behind the RAPID tomographic algorithm is briefly reported in this section, along with a critical discussion of the advantages and the disadvantages related to the employment of such a reconstruction method. The whole procedure is presented concerning a plate-like structure whose properties are defined in section 3.1.

2.1 Theoretical description

The RAPID algorithm is founded on the physical fact that as the propagating LW encounters a defect, mode conversion and wave reflections will take place. The installation of a sensing network on the structure allows recording the Lamb Waves propagating signals at different stages, which are later employed in the subsequent post-processing aimed at detecting and localising eventual damages. A proper statistical comparison of the healthy baseline with the currently acquired pattern is required for a correct structural health assessment, based on a metric defined exploiting a properly set up feature extraction process. One example is the so-called signal difference coefficient (SDC), often computed based on the Pearson coefficient [20], [21]. Hence, Pearson coefficient-based SDC is selected in this paper as Damage Index (DI) to be implemented in the RAPID algorithm, rather than other comparable solutions such as the signal sum of squared differences and the discrete wavelet transform. According to preliminary analyses performed for setting up this work, which are not reported here for the sake of brevity, Pearson coefficient-based SDC is believed to provide the most satisfactory tomographic results when dealing with LWs-based SHM. The damage index formulation considered in this work is reported in equation (1).

$$DI_k = 1 - \frac{\sum_{i=1}^{n}\left(S_{H,i} - S_H\right)\left(S_{D,i} - S_D\right)}{\sqrt{\sum_{i=1}^{n}\left(S_{H,i} - S_H\right)^2}\sqrt{\sum_{i=1}^{n}\left(S_{D,i} - S_D\right)^2}} \quad (1)$$

Where S_H and S_D represent the lamb waves signals recorded as healthy baseline and on the possibly damaged structure currently investigated, respectively, while n is the number of data points acquired during the interrogation phase. The interrogation technique utilised in this article is based on the pitch-catch procedure, for which one of the piezoelectric sensors (PZT) of the

sensor array operates as an actuator and the rest measure the propagating signal. Each interrogation database is composed of several paths, one for each actuator–sensor pair. Accordingly, one DI can be computed for each path, which allows quantifying the corresponding damage level.

Moreover, the RAPID algorithm further post-processes the DI values and assigns a damage probability to each pixel into which the structure under assessment is discretised. Zhao et al. [13] stated that the signal would be more disturbed when the defect is placed on the direct path, i.e., straight line joining the actuator–sensor pair. Hence, a weighted probability distribution is needed to account for the effect of the defect position relative to the PZT pair. The authors proposed an elliptical-shaped probability distribution in which the PZT pair represents the ellipse foci, with the greatest probability assigned to the ellipse major axis, i.e., direct path. The estimated probability decreases as the relative position of the pixel considered approximate to the ellipse perimeter. The equations dictating this elliptical distribution is then weighted by the DI for each path considered. The output result is a tomography in which an estimated probability of defect is assigned to each pixel, i.e., to each discretised geometrical point, according to equation (2).

$$\begin{aligned} P(x,y) &= rescale\left(\sum_{k=1}^{n_p} DI_k\left(\frac{\beta - R_k(x,y)}{\beta - 1}\right), [0,1]\right) \\ &= rescale\left(\sum_{k=1}^{n_p} DI_k I_k(x,y), [0,1]\right) \\ &= rescale\left(\sum_{k=1}^{n_p} P_k(x,y), [0,1]\right) \end{aligned} \quad (2)$$

Where n_p is the total number of paths and β is a scaling parameter controlling the size of the minor axis of the ellipse. This parameter should be adjusted for each case study. In fact, if this parameter is too low, artefacts may appear, thus leading to false defect estimations. On the contrary, if β is too high, resolution may be lost. The $R_k(x,y)$ value involved in equation (2), which acts as a measurement of the relative distance between the analysed pixel and the direct

path between the pair of sensors, is defined through equation (3), where (x_i, y_i) and (x_j, y_j) are the coordinates of the ith PZT sensor and jth PZT actuator, respectively.

$$R_k(x,y) = \begin{cases} \dfrac{\sqrt{\left(x - x_i + \alpha(x_i - x_j)\right)^2 + \left(y - y_i + \alpha(y_i - y_j)\right)^2} + \sqrt{\left(x - x_j + \alpha(x_j - x_i)\right)^2 + \left(y - y_j + \alpha(y_j - y_i)\right)^2}}{\sqrt{\left(x_i - x_j - 2\alpha(x_i - x_j)\right)^2 + \left(y_i - y_j - 2\alpha(y_i - y_j)\right)^2}} & for R_k(x,y) < \beta \\ \beta & for R_k(x,y) \geq \beta \end{cases} \quad (3)$$

The coefficient α was introduced by Moix-Bonet et al. [21] to drop the false high probability created by the overlap of the ellipse extremes at the PZT locations. This parameter should be also tuned for each case analysed, since a low value might create false probability "hot-spots", while a large value might reduce the effective search area nearby the sensors, i.e., a defect placed close to a sensor may not be detected.

Combining equations (2) and (3), the damage probability at a pixel (x, y) is determined by the summation of the paths contributions $DI_k I_k$ over all the PZT paths, where the contribution of the kth path is constrained within the corresponding ellipse defined by the scaling parameter β; outside this ellipse, i.e. if $R_k(x, y) \geq \beta$, the respective estimated probability $P_k(x, y)$ equals zero. An image of the overall graphical description of the estimated probability distribution for a generic path joining actuator i and sensor j is shown in Figure 1.

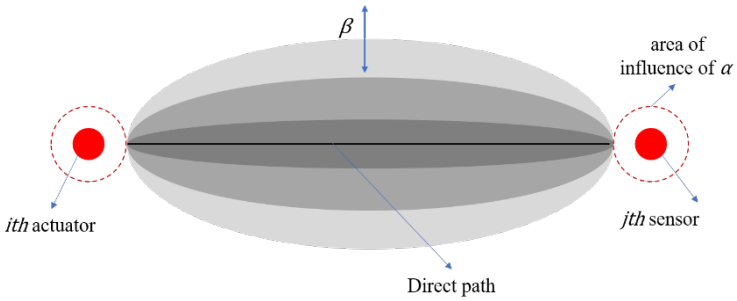

Figure 1. Probability distribution of the modified RAPID algorithm.

2.2 *RAPID critical discussion*

Although the algorithm discussed above is easily implementable, it also presents some flaws that cannot be neglected for the correct implementation of the method and interpretation of the results.

The false probability "hot-spots" created by an uneven sensing network is one of the most critical flaws, since it may significantly increase the number of false detections or, simply, decrease the localisation accuracy of the real damage. This issue is determined by the recurrent overlap of probability ellipses when the contributions of every path are added together. The higher the number of ellipses intersecting at one pixel, the larger the estimated probability at this pixel. This may lead to higher values than the actual ones coming from high damage index values due to real damage onset, thus leading to bad diagnosis performance. In Figure 2, the direct paths pertaining to each sensors pair and the total unweighted probability distribution $UP(x,y)$ are shown for star, rectangular and circular sensors arrangements of 8 PZTs each. Particularly, $UP(x,y)$ was computed by means of equation (4). This matrix is intrinsic to the method employed since several ellipses with diverse probabilities are added sequentially. Note that matrix $UP(x,y)$ is equivalent to the tomography matrix $P(x,y)$ without the term related to the damage index.

$$UP(x,y) = \sum_{k=1}^{n_p} \left(\frac{\beta - R_k(x,y)}{\beta - 1} \right) = \sum_{k=1}^{n_p} I_k(x,y) \qquad (4)$$

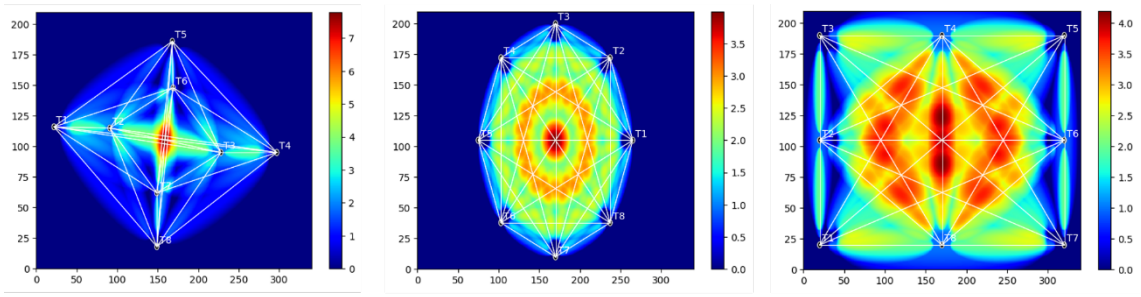

(a) (b) (c)

Figure 2. Sensing network density with $\boldsymbol{\alpha = 0.08}$ and $\boldsymbol{\beta = 1.03}$ for (a) star sensors arrangement, (b) circular sensors arrangement and (c) rectangular sensors arrangement.

It can be appreciated that in the areas where the ellipses intersect the most, the probability value is biased. If the difference between the healthy and the damage signals is not high enough to produce high damage index values that successfully drive the damage probability estimations towards pixels close to the real damage, the tomography maxima will tend to be drawn towards the red areas identified in Figure 2. This statement is graphically explained in Figure 3, where the original RAPID algorithm is applied to the star sensor arrangement for $\alpha = 0.08$ and $\beta = 1.03$. Hereinafter, the real damage is represented using a white circle within the tomography while the predicted damage is indicated through a black cross representing the pixel of maximum probability given by the localisation algorithm. For the star configuration shown in Figure 3, the number of intersections passing through the central area is very high. As reasoned above, the summation of ellipses inherent in the RAPID algorithm will generate a situation in which even low values of the DIs would wrongly position the maxima of the estimation within this central area. In this case, the very high DI of the paths T1-T7 and T2-T8 (i.e., the direct paths crossing the real damage) is not enough to overcome the effect of the high number of intersections, thus leading to a counter-intuitive localisation result and to a bad diagnostic performance.

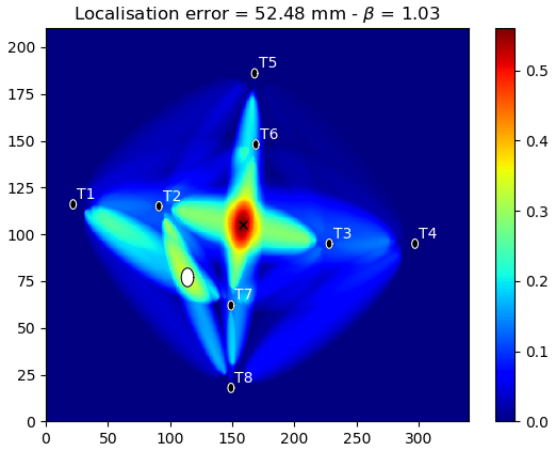

Figure 3. Original RAPID tomography for star sensor arrangement with $\boldsymbol{\alpha = 0.08}$ and $\boldsymbol{\beta = 1.03}$

As mentioned above, the original version of the RAPID algorithm is intrinsically bonded to the characteristics of the probability ellipses. The shape of these ellipses, at the same time, is defined by the parameter β and, to a lesser extent, by the parameter α. The designer of the localisation algorithm must initialise these two parameters introducing, therefore, subjectivity in the analysis, although some guidelines can be given based on experience. First, the value of α should be high enough to avoid the overlap of the ellipses extremes close to the PZT sensors, even though an excessively large α value prevents the localisation of damages arising near the sensors. Second, the definition of the parameter β involves an iterative process to find the value that yields the best results and a trade-off should be reached to properly define β. A low value would produce slim ellipses, thus not effectively interrogating the complete potential scanning area, incurring in larger estimation errors, while large values may cause a loss of resolution. The latter effect becomes particularly critical when several damages are present on the structure since the large probability zones could excessively overlap.

Furthermore, the optimal α and β are dependent on the sensors arrangement, on the geometry of the structure and, to a lesser extent, on the damage dimensions. The latter being an unknown variable, α and β are usually initialised only considering the structure geometry and the sensor arrangement and remain unchanged during the entire service life. The effect of considering different β values on the tomographic results are graphically explained in Figure 4for the case of a circular sensors arrangement. From Figure 4a, it can be appreciated how the high probability area is very constrained, but the estimation error is high since the ellipses do not uniformly cover the interrogation area. Contrarily, in Figure 4b a larger β value is considered, which allows uniformly covering the interrogating area and reducing the localisation error while increasing the size of the red high probability area due to the excessive overlap of the ellipses pertaining to the sensors paths.

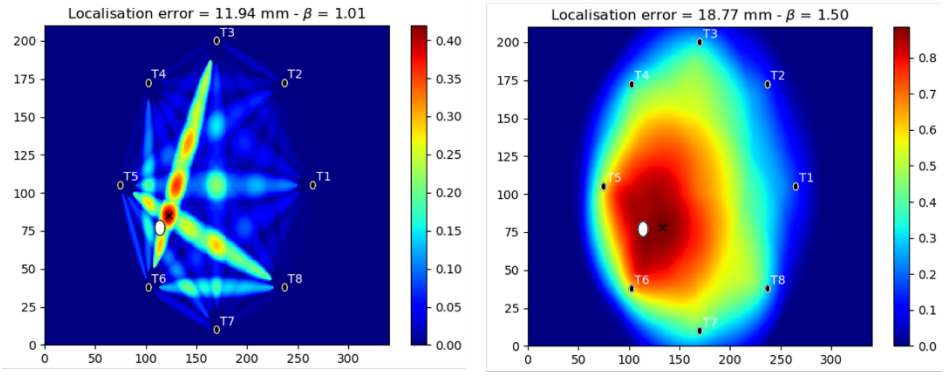

(a) (b)

258

259 **Figure 4.** Effect of $\boldsymbol{\beta}$ for the circular sensor arrangement. (a) $\boldsymbol{\beta = 1.01}$ and (b) $\boldsymbol{\beta = 1.5}$

260

261 In the present work, the value of α is iteratively searched to find the minimum value that allows
262 avoiding the overlap of the ellipses extremes without losing scanning area. The optimum
263 parameter value is identified in $\alpha = 0.08$.

264 The iterative process to select β is based on the minimisation of an optimisation index, $OI(\beta)$,
265 which depends on two terms that quantitatively represent the effect of β on the tomographic
266 images. The first term is the localisation error, computed as the distance between the RAPID-
267 estimated maximum damage probability and the centre of the damage ,err_{loc}, which is normalised
268 through a division by the panel diagonal length. This normalisation process was applied in order
269 to have comparable values of the two optimisation terms. Within the context of this work, OI(β)
270 was employed to provide a less biased comparison between the original RAPID algorithm and
271 the proposed enhancement, thus the real damage position is known a priori. It should be clarified
272 that this term could not be considered in those scenarios where the damage has not been localised
273 yet. The second term is the number of pixels n_{HP} from the normalised tomography that meets the
274 condition $P_k(x, y) > 0.7$, identifying the extent of the high damage probability area. A sensitivity
275 analysis of the limit value of $P_k(x, y)$ was performed to determine the most suitable values. This
276 analysis is not presented here for the sake of brevity. The optimisation index is then computed as
277 expressed in equation (5).

$$OI(\beta) = C_1 err_{loc} + C_2 n_{HP} \quad (5)$$

With $C_1 + C_2 = 1$. These two coefficients weigh the importance that the user gives to each term. In fact, a large value of C_1 means that the localisation error weights more for the selection of β, while a large value of C_2 identifies an algorithm resolution-driven optimisation. For the present work, the values $C_1 = 0.7$ and $C_2 = 0.3$ were selected. These coefficients were iteratively modified until an acceptable trade-off between the optimisation terms allowed giving slightly more importance to the localisation error.

Finally, the RAPID algorithm was iteratively applied considering values of β ranging from 1.01 to 1.50, with step 0.01, keeping a constant value of $\alpha = 0.08$. The value of β yielding the minimum $OI(\beta)$ was selected. It is thought that the implementation of this optimization process helps to provide a less biased comparison between the original RAPID algorithm and the proposed modification since the optimum β value is independently selected for each one of the two methods.

2.3 RAPID algorithm proposed improvement

The uneven sensing network density is addressed by reducing the artificial probabilities created by the recurrent overlap of the probabilistic ellipses. Logically, the higher the number of ellipses overlapping at pixel (x, y), the higher the falsely estimated probability $P(x, y)$ even in absence of close damage. Similarly, the false probability is higher for areas in which the ellipses major axis, i.e., direct paths, intersects due to different probabilities within the ellipse, as noticed in Figure 1. Therefore, the exposed problem is reduced to finding the number of intersecting ellipses at each pixel on the discretised structure and, accordingly, lowering the damage probability value. The RAPID algorithm used in the present work as well as the proposed modifications are implemented in the Python coding language.

The structure is represented using a mesh where each point represents a pixel in the final tomography. Each pixel is assigned a value $R_k(x, y)$ according to equation (3). A unit value is

assigned to the pixels with a non-zero $R_k(x,y)$, while the pixels outside the kth ellipse are given a null value. These computed values, pertaining to the kth path, are stored in a matrix $INTER_k$, each element of which corresponds to a pixel in the mesh discretisation and identifies whether that pixel lies inside or outside the kth ellipse. This process is repeated for all the n_p paths and, finally, the matrix counting the number of ellipses passing through each pixel is constructed according to equation (6).

$$INTER = \sum_{k=1}^{n_p} INTER_k + 1 \tag{6}$$

A unitary value is added up to each element of the $INTER_k$ matrix to avoid singularities in the subsequent mathematical operations involving element-by-element division by the matrix $INTER_k$. The unbiased damage probability P_{UNB} is then obtained by the element-by-element division of the matrix P, which stores the damage probability value $P(x,y)$ computed at each pixel of the plate (refer to equation (2)), by the matrix $INTER$, as shown in equation (7). Consequently, the effect of ellipse overlap is attenuated, leaving the augmented estimated probability unmodified due to the consideration of the damage index.

$$P_{UNB} = P./INTER \tag{7}$$

A blur filter is also introduced to damp out eventual artificial sharp peaks introduced during the step one of the procedure. The blur filter adopted in this work filters the unbiased damage probability matrix P_UNB with a 2-D Gaussian convolution matrix (or kernel). This means that the pixel under consideration is averaged by considering the neighbouring pixels or, in other words, the pixels within the kernel limits. The weight of each pixel within the kernel, over which the average value is computed, is determined according to the Gaussian distribution shown in equation (8):

$$G(x,y) = \frac{1}{2\pi\sigma^2} e^{-\frac{(x-x_C)^2+(y-y_C)^2}{2\sigma^2}} \tag{8}$$

where $G(x, y)$ is the weight associated to each pixel within the kernel and σ the standard deviation assigned to the kernel. Note that x_C and y_C are the coordinates of the kernel central pixel. In the present work, the standard deviation was set to 5 and the kernel size was 21 pixels x 21 pixels. These values were found to be small enough not to lose resolution due to excessive blurring and high enough to have a correct smoothing of the tomography. The implemented filter was applied to P_{UNB} obtaining as output the enhanced damage probability matrix P_{ENH}.

3 Case study

This section introduces the numerical model developed to show the capabilities of the proposed enhanced RAPID algorithm and reports a critical discussion of the results of the tomographic assessment.

3.1 Numerical model

The algorithm proposed in the present work relies on the information gathered from the comparison of the healthy baseline and the current, possibly damage-modified signals. Therefore, to analyse the performance of the proposed improvement, a healthy and damaged database, containing the propagation signals for each path, must be created. These databases should allow the capture of the signal differences generated by the defect rather than describing the complete physical propagation process. It has been stated in several studies ([7], [22], [23]) that FE models can be used as predictive tools for the analysis of LWs-based SHM systems. In spite of the fact that experimental validation is always needed, the use of numerical models greatly widens the range of case studies that are susceptible to be implemented, making the whole study very cost-efficient compared with experimental tests. In this work, it is thus proposed to use an FE-based model implemented in ABAQUS/Explicit for the performance evaluation of the proposed RAPID algorithm.

A CFRP prepreg CYCOM® 977-2-34%-24K IMS-196-T1 panel made of 18 unidirectional layers with layup $[45^o, -45^o, 0^o, 45^o, (-45^o)_2, 45^o, 90^o, 0^o]_S$ is taken as the reference model. The material properties are shown in Table 1. All the shown properties are experimentally obtained according to the operative procedures reported in the last column of Table 1. It is worth mentioning that, as is discussed below in this Section, a shell-based model is used, therefore only the in-plane elastic parameters are needed.

Table 1. CFRP properties implemented.

Lamina Properties	Value	Obtaining procedure
Density	$\rho = 1620\, kg/m^3$	Rule of mixture
Longitudinal and transverse moduli	$E_1 = 157.5GPa; E_2 = 9.9GPa$	ASTM D3039
Shear modulus	$G_{12} = 4.95GPa$	ASTM D3518
Poisson's ratio	$v_{12} = 0.24$	ASTM D3039

The overall dimensions of the panel are 340mm x 210mm x 3.8mm. It was assumed that the panel was rigidly fixed using two steel frames that clamped the specimen. This boundary condition was numerically replicated by fixing all 6 degrees of freedom of all the outermost nodes.

The number of PZT sensors modelled was 8, thus leading to 56 sensing paths, i.e., $N \cdot (N-1)$, being N the number of PZTs. In total, 16 simulations (i.e., 8 actuators for healthy and 8 ones for damage conditions) were run for each sensor arrangement and each damage considered. Consequently, it was decided to adopt a layered-shell model typology, which also considers the large in-plane dimensions of the panel. The layup was then considered through the definition of the different integration points properties rather than the explicit consideration of each layer as a single part as performed in the 3D stacked-solid model. It is also worth mentioning that the scope of the present study is the performance evaluation of the proposed improvement on the RAPID algorithm rather

than the creation of an accurate numerical model. For the aim of this paper, a numerical model able to capture the LWs propagation differences in healthy and damage scenarios is believed to be sufficient.

The PZT sensors were modelled using 3D solid elements with 1 integration point and 8 nodes. The modelling strategy was based on the work presented in [24], with the exception that the elastic behaviour of the PZT sensors was considered to be transversely isotropic. Figure 5 shows the stiffness matrix adopted.

$$C = \begin{bmatrix} 136.33 & 71.68 & 68.63 & 0 & 0 & 0 \\ & 136.33 & 68.63 & 0 & 0 & 0 \\ & & 118.28 & 0 & 0 & 0 \\ & & & 32.33 & 0 & 0 \\ & Sym. & & & 28.01 & 0 \\ & & & & & 28.01 \end{bmatrix} GPa$$

Figure 5. Stiffness matrix of the PZT sensor.

The excitation used was made up of a tone burst with 3 periods with a central frequency equal to 250kHz. The excitation was reproduced numerically by imposing the radial displacement to the outermost nodes of the uppermost perimeter of the PZT cylindrical part, as highlighted in red in Figure 6. This is coherent with the fact that the commonly used PZT type works in the radial extensional mode. The PZT numerical parts were rigidly tied to the composite shell part. A representation of the final model with the PZT component highlighted is presented in Figure 6.

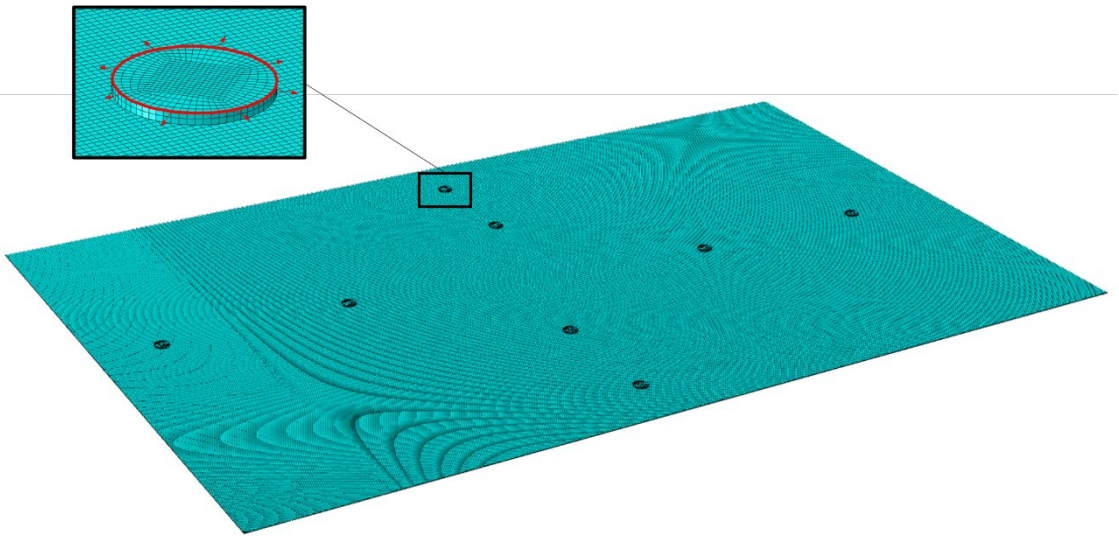

Figure 6. Numerical model: mesh and imposed displacement.

Several authors ([8], [10], [22]) have stated that one of the most critical factors during the simulation of the LWs propagation phenomenon using the FE method is the proper selection of the mesh dimension. It must be ensured that the size of a model region made up of 6 to 12 elements is approximately equal to the smallest wavelength involved in the propagation. At the same time, the wavelength is directly related to the propagation velocity. One can thus use equation (8) to compute the maximum allowable element dimension as:

$$l_{max} = \frac{\lambda_{min}}{n_{min}} = \frac{c_{min}}{n_{min} \cdot f_{exc}} \quad (9)$$

where λ_{min} is the smallest wavelength, n_{min} is the user-defined number of nodes per wavelength, which is suggested to be between 6 and 12, c_{min} is the minimum propagation velocity encountered in the case study and f_{exc} the excitation frequency. In the present study, c_{min} is computed by plotting the dispersion curves using the free available software Dispersion Calculator [25]. The heterogeneous nature of composite materials is translated into a non-isotropic behaviour of the panel, consequently, the wave propagation velocity may be affected by the propagation direction in the case of composite materials. The larger the stiffness, the larger the propagation velocity. One can thus expect a faster propagation along the predominant fibre

directions. In order to observe this dispersive behaviour, the polar plot for an excitation frequency of 250kHz is presented in Figure 7.

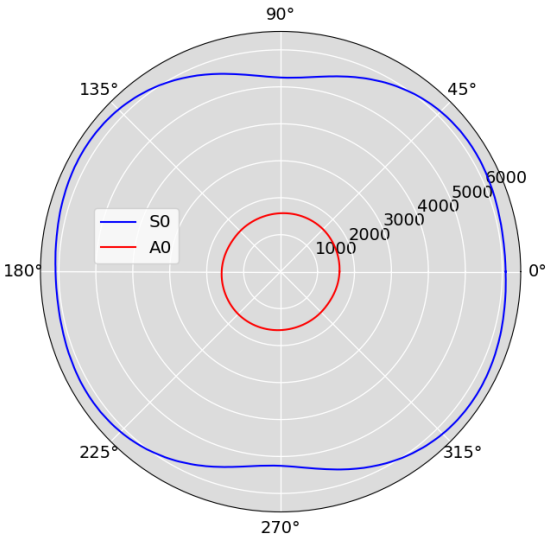

Figure 7. Effect of propagation direction in group velocity for an excitation frequency of 250kHz. Velocities are expressed in m/s.

Due to the circular shape of the A_0 mode profile, this mode is not significantly affected by the material anisotropy. This behaviour is expected due to the quasi-isotropic characteristic of the panel simulated. In any case, the slowest group velocity was equal to 1550 m/s. This value is then set as c_{min} in equation (7). Knowing that f_{exc} is equal to 250kHz and selecting a n_{min} of 12, the calculated l_{max} was equal to 0.52mm. However, to be conservative and to have a constant element dimension along the panel length and breadth, a smaller mesh dimension acting as a common denominator of the two plate dimensions is chosen, i.e., 0.25mm. In any case, a mesh sensitivity analysis is performed to assess the validity of this choice. Figure 8 depicts the propagation signal for the pair actuator-receiver T2-T8 (refer to Figure 10 for sensor identification). The average radial strain on the surface of the PZT part directly in contact with the composite part was taken as the output signal. This choice is also coherent with the working principle of the PZT selected, i.e., radial extensional mode. Figure 8 clearly shows that, as far as the mesh dimension is kept below the limit value, i.e. 0.52mm, the output signal differences are negligible.

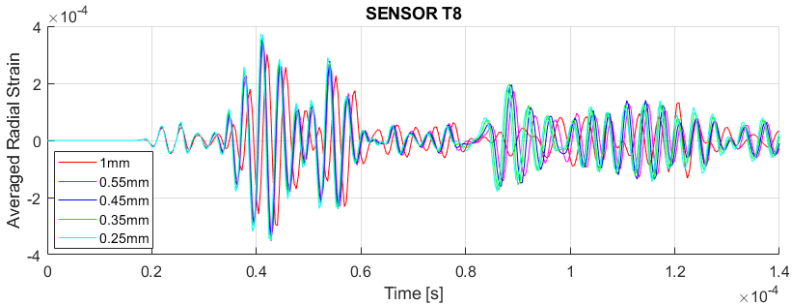

Figure 8. Mesh sensitivity analysis: actuator T2 and sensor T8.

3.2 Enhanced RAPID algorithm performance

The model presented in Section 3.1 is used to test the performance of the proposed algorithm. In particular, the healthy baseline is acquired by propagating the LWs in the plate shown in Figure 6. The damage condition has been simulated by introducing a through-thickness hole in 2 different positions and with 2 different diameters as illustrated in Figure 9. It should be emphasised that the study of the influence of different damage typologies on the RAPID algorithm is out of the scope of the present article. Consequently, the authors decided to consider a through-thickness hole for its simplicity and proved efficiency when used on FEM modelling. For the relative position of these damages with respect to the different sensor configurations one should refer to Figure 12 and Figure 13.

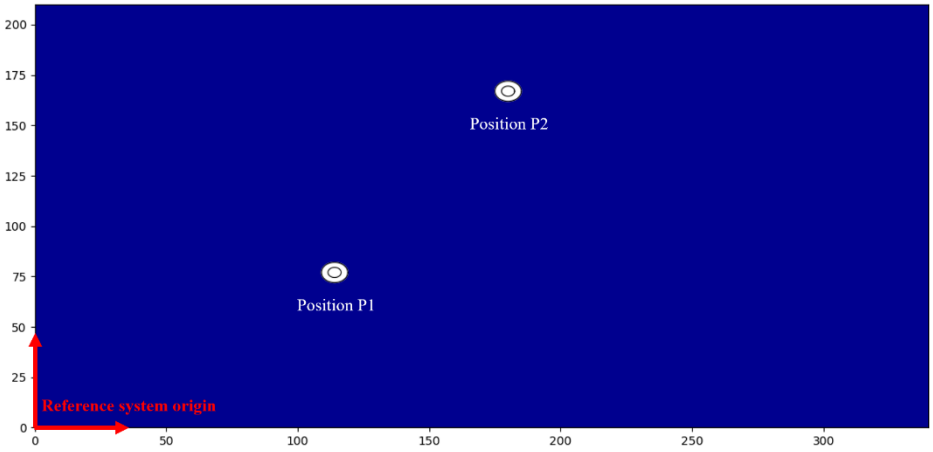

Figure 9. Damage position.

Moreover, the performance of the enhanced RAPID algorithm is assessed considering three different sensors arrangements, i.e, the star, the rectangular and the circular layout. All the configurations are characterized by the presence of 8 sensors, one at a time acting as actuator during the signals acquisition process according to the so-called pitch-catch technique. In Figure 10, the sensors arrangements and the coordinates of each PZT centre are shown.

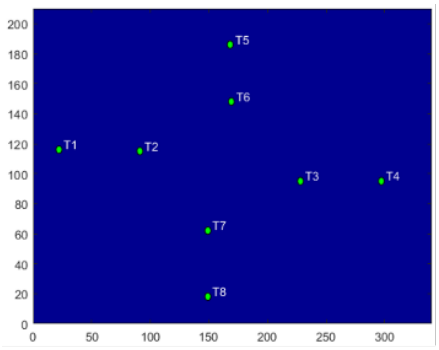

(a)

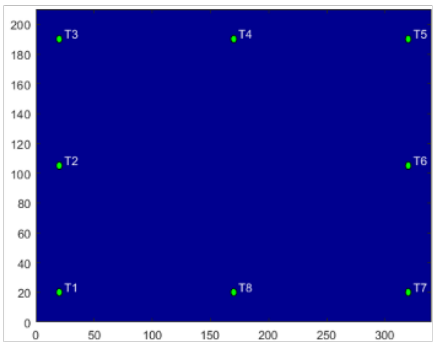

(b)

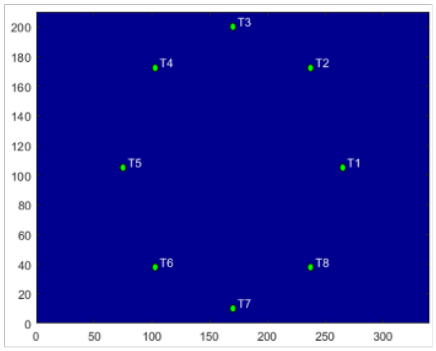

(c)

Sensor ID	Star arrangement	Rectangular arrangement	Circular arrangement
T1	(22, 116)	(20, 20)	(265, 105)
T2	(91, 115)	(20, 105,)	(237, 172)
T3	(228, 95)	(20, 190)	(170, 200)
T4	(297, 95)	(170, 190)	(103, 172)
T5	(168, 186)	(320, 190)	(75, 105)
T6	(169, 148)	(320, 105)	(103, 38)
T7	(149, 62)	(320, 20)	(170, 10)
T8	(149, 18)	(170, 20)	(237, 38)

(d)

Figure 10. Sensor arrangements implemented. (a) Star, (b) rectangular, (c) circular sensor arrangements and (d) coordinates of the centre of each sensor.

For the sake of clarity, each damage has been analysed individually. Consequently, 4 different numerical damage databases have been created. A summary of all the simulations performed in this work is presented in Table 2, where an ID in the form *PiXj* is assigned to each analysis, where *Pi* identifies the damage position, i.e., $i = 1,2$ (Figure 9), *X* the sensors arrangements initial letter, i.e., S for the star, C for the circular and R for the rectangular arrangement, and *j* the damage size in mm, i.e., $j = 5,10$.

Table 2. Simulations performed.

Sensors arrangement	ID	Hole diameter [mm]	Hole position (x, y) [mm]

Star	P1S10	10	(114, 77)
	P1S5	5	(114, 77)
	P2S10	10	(180, 167)
	P2S5	5	(180, 167)
Circular°	P1C10	10	(114, 77)
	P1C5	5	(114, 77)
	P2C10	10	(180, 167)
	P2C5	5	(180, 167)
Rectangular	P1R10	10	(114, 77)
	P1R5	5	(114, 77)
	P2R10	10	(180, 167)
	P2R5	5	(180, 167)

459

460 The real scanning area is discretised to have square pixels with dimensions 0.5x0.5mm^2. The final
461 dimensions of the tomography matrix are 680 pixels x 420 pixels. These dimensions are a good
462 trade-off between computational cost and resolution quality.

463 The damage localisation error, measured in mm, is considered as a relevant metric to fairly
464 compare the results obtained employing the original RAPID algorithm with those from the
465 enhanced version proposed in this work. The damage localisation error is defined as the distance
466 between the centre of the real damage and the coordinates of the maximum damage probability
467 calculated by the algorithm.

468 A summary of the results is reported in Table 3. As already mentioned in section 2.2, the
469 parameter β is chosen within the range [1.01; 1.5] through an optimisation process. According to

equation (5), The selection is performed so that the localisation error is more heavily weighted compared to the tomographic resolution. For this purpose and as stated in Section 2.2, the weight associated with the localisation error (C_1) is 0.7 in comparison with the weight 0.3 given to the term associated with the resolution performance (C_2). The purpose of this choice is to ease the comparison of the performances of the original and the enhanced RAPID (hereinafter referred to as E-RAPID) algorithms. As it can be seen from Table 3, each sensor layout is given its own optimum β parameter value, thus the optimization algorithm has been run for each new database. Instead, the parameter value $\alpha = 0.08$ is found to work well for all the cases, hence it is kept constant throughout the different analyses.

The results are reported in Table 3.

Table 3. Results and comparison.

	d_{hole} = 10mm; (x, y) = (114, 77)mm (P1)				
	Original		Enhanced		Improvement
	Error [mm]	B [-]	Error [mm]	B [-]	[%]
Star	22.73	1.28	0.38	1.02	98.33
Circular	11.94	1.01	4.88	1.18	59.13
Rectangular	6.18	1.01	3.25	1.02	47.41

	d_{hole} = 5mm; (x, y) = (114, 77)mm (P1)				
	Original		Enhanced		Improvement
	Error [mm]	B [-]	Error [mm]	B [-]	[%]
Star	24.21	1.31	0.46	1.03	98.10
Circular	11.94	1.01	4.88	1.18	59.13
Rectangular	6.24	1.15	9.50	1.32	-52.24

	d_{hole} = 10mm; (x, y) = (180, 167)mm (P2)				
	Original		Enhanced		Improvement
	Error [mm]	B [-]	Error [mm]	B [-]	[%]
Star	9.56	1.15	5.91	1.21	38.18
Circular	4.78	1.05	4.52	1.02	5.44
Rectangular	16.83	1.22	31.12	1.29	-84.91

	d_{hole} = 5mm; (x, y) = (180, 167)mm (P2)				
	Original		Enhanced		Improvement
	Error [mm]	B [-]	Error [mm]	B [-]	[%]
Star	10.04	1.12	6.31	1.21	37.15
Circular	6.58	1.02	4.96	1.02	24.62
Rectangular	9.95	1.49	30.84	1.03	-209.94

The improvement has been computed as the percentage of change in the localisation error distance for the E-RAPID in comparison with RAPID. First, the uneven sensing network density issue needs to be analysed in detail. The matrix $INTER$ (see Section 2.3) is represented graphically in Figure 11 for a constant value of $\beta = 1.03$, to point out the number of intersections at each pixel of the plate, as well as the most intersected areas for each sensors arrangement. The star sensor arrangement is the configuration that provides the largest number of intersections. Specifically, most of the paths cross the monitored area centre, thus misleadingly increasing the estimated probability on the central area of the panel. Accordingly, for the case in which the damage index values are not high enough to dominate the prediction of the algorithm damage prediction, the maxima of the original RAPID algorithm would potentially be drawn towards the centre as graphically stated in Figure 3. Moreover, for damage positions close to the centre, yet not exactly in the centre, a bias in the localisation prediction is expected, since centre-crossing paths would be assigned with high damage index values, further increasing the damage probability at the exact centre of the panel and not at the real nearby position. Partially, the same argument can be applied to the circular arrangement, which presents a large number of highly intersected hot spots, artificially deviating the localisation error estimation. Differently, the rectangular arrangement seems to be the best choice with regard to the uniformity of the sensing network density. In fact, Figure 11 and Figure 2 show that this configuration presents both the most homogeneous intersection matrix and the most uniform distribution of unweighted probability. This fact is believed to have caused the worst performance of the E-RAPID algorithm in comparison with the original one, as observed in Table 3. The intrinsic uniformity of the sensing network density given for the rectangular configuration makes the use of the E-RAPID algorithm less necessary. The proposed improvement is therefore aimed at highly irregular sensors arrangements such as the case of the star and, to a lesser extent, the circular one. Indeed, observing the results of Table 3, the star configuration provides the best results for all the cases, achieving a maximum improvement of 98.33%. It should be kept in mind that the actual implementation of a sensing network on a real aeronautical structure is always subjected to several restrictions such as

geometrical joints or discontinuities. Consequently, the installation of a uniform sensing network is not always possible.

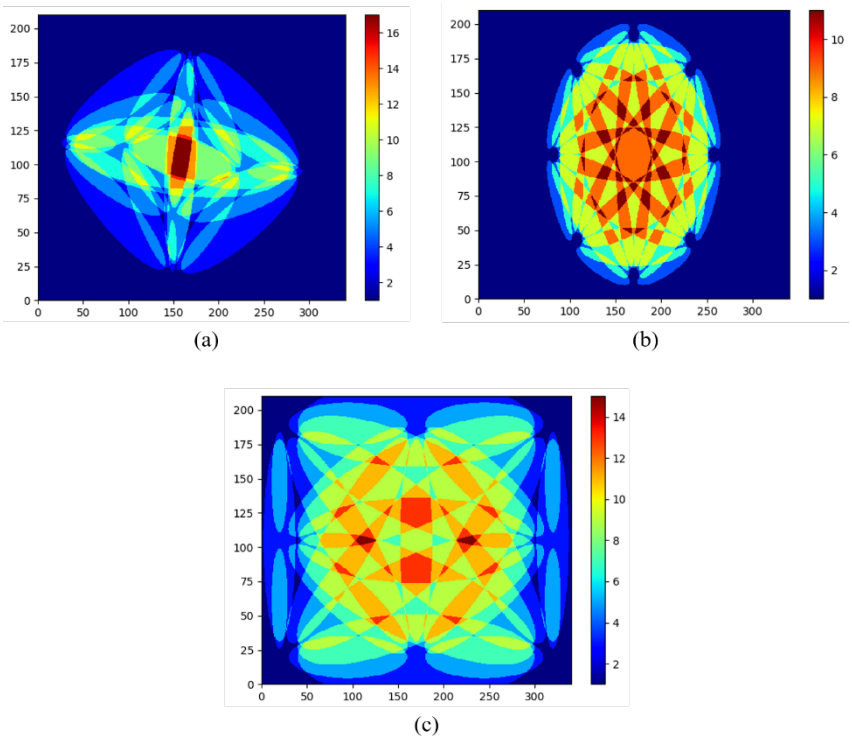

Figure 11. Intersection matrices for (a) star, (b) circular and (c) rectangular sensor arrangement

A detailed comparison of the performances of the original and of the enhanced RAPID algorithms is reported in Figure 12 considering the star and the circular sensors arrangements.

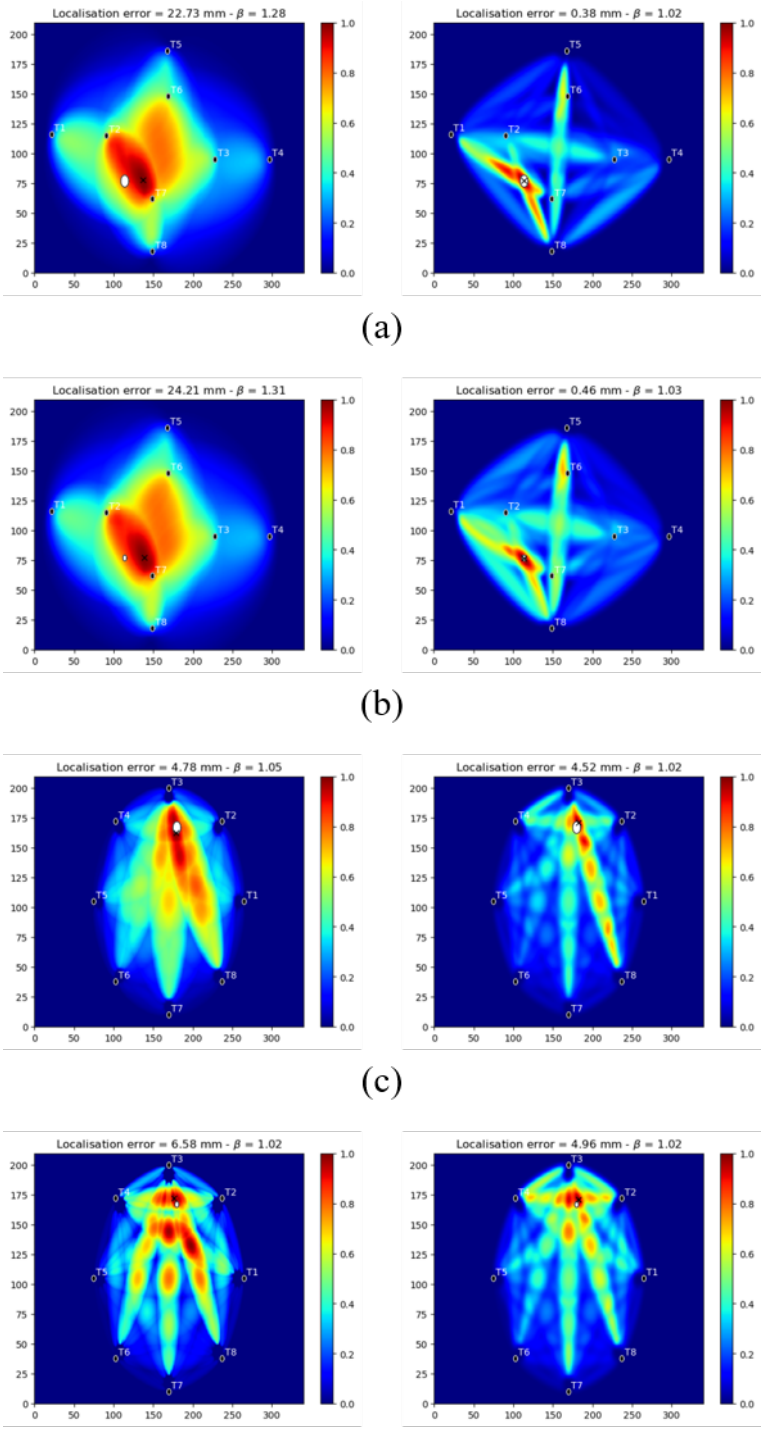

Figure 12. Tomographies for original RAPID (left) and E-RAPID (right) for simulations (a) P1S10, (b) P1S5, (c) P2C10 and (d) P2C5.

Observing the tomographies for the star configuration depicted in Figure 12a and Figure 12b, a clear improvement both in terms of localisation and in the algorithm resolution can be seen. The

highly intersected area in the centre of the star configuration created a significant hot-spot which prevented the original RAPID algorithm from having a low localisation error with appropriate resolution. The averaging of the tomography matrix proposed here reduced the central hot spot, as can be seen in Figure 11a, thus allowing for a proper weighting of those paths with larger damage indexes. Consequently, employing the E-RAPID algorithm allowed achieving results in the best performance in terms of localisation error at low values of β, thus preserving high resolution.

Regarding the circular sensor arrangements, whose tomographies are illustrated in Figure 12c and Figure 12d, the same argument can be applied both for the 10mm hole and for the 5mm one. Interestingly, Figure 12d shows that the optimisation algorithm found the same β for both the original RAPID and the E-RAPID. However, even if the optimum β is the same, the use of the $INTER$ matrix and Gaussian filtering allowed to achieve, again, a lower localisation error with an improved resolution.

As said above, the use of E-RAPID over the original algorithm is more justified for the sensor arrays which present a higher density unevenness. This is coherent with the results presented in Table 3, where the highest percentage of improvement is attributed to the most irregular network layout, i.e., the star one, less pronounced for the circular one and not present for the rectangular layout. In fact, apart from the P1R10 simulation, the application of the E-RAPID algorithm worsened the localisation error for the rectangular arrangement. As an example, the localisation results for the P2R10 simulation are shown in Figure 13.

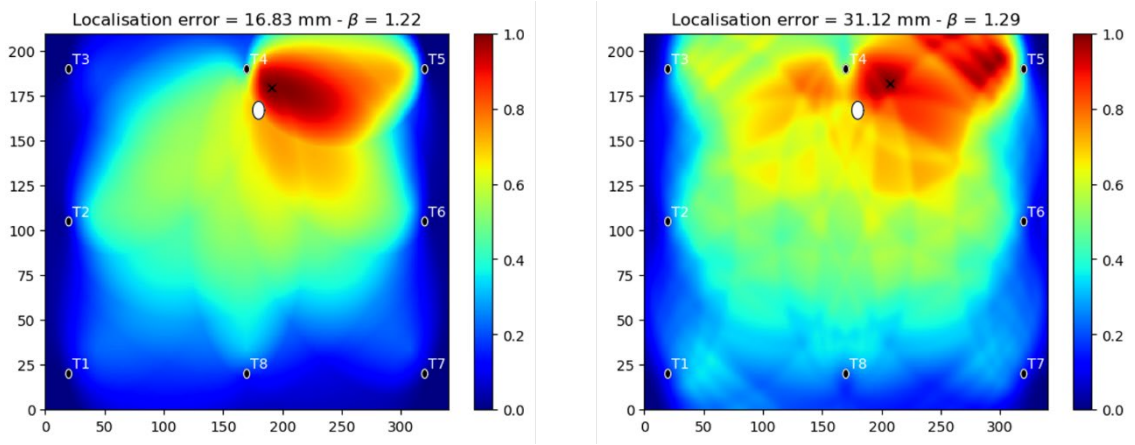

545

546 **Figure 13.** Result tomography for the simulation P2R10. Original RAPID (left) and E-RAPID (right).

547

548 The factor causing the low localization precision observed in Figure 13 is thought to be related to
549 the intrinsic inhomogeneity of the $INTER$ matrix, graphically exposed in Figure 11, which even
550 though it has been partially dealt with employing the gaussian blur filtering technique, it still
551 influences the damage diagnosis task for the rectangular arrangement. In this case, the lowest
552 inhomogeneity of the sensing network density combined with the inhomogeneity of the
553 intersection matrix generated that the largely intersected areas were excessively averaged in
554 comparison with the lowest intersected ones. The previous discussion aimed to highlight the
555 eventual disadvantages of the method proposed for opening the possibility of future
556 improvements.

557 As stated throughout the present article, the value of the parameter β is of outmost importance for
558 the working principle of both the RAPID and the E-RAPID algorithms and, consequently, special
559 attention is needed. With the purpose of fairly showing the validity of the proposed method, the
560 results shown in Figure 12 are reproduced in Figure 14 considering a constant β=1.01, that is,
561 without applying the optimisation method proposed in equation (5). Regarding the rectangular
562 configuration, no improvement was observed with constant β since the same statement made
563 above is still valid. Consequently, and for the sake of conciseness, the results for the rectangular
564 configurations are not presented here.

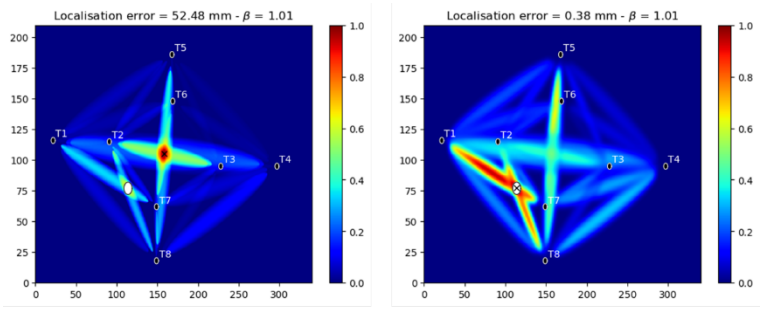

(a)

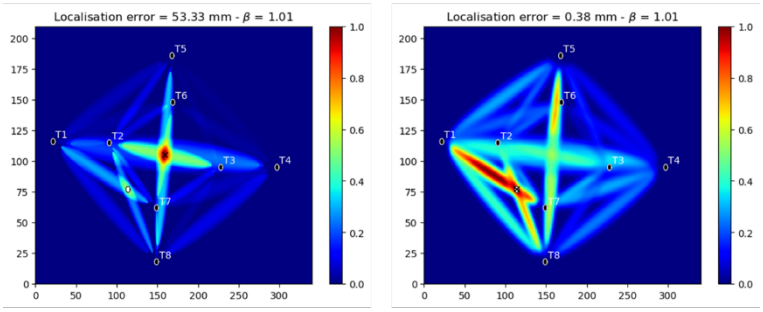

(b)

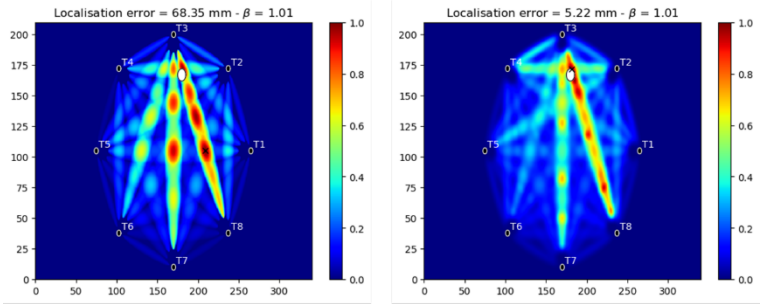

(c)

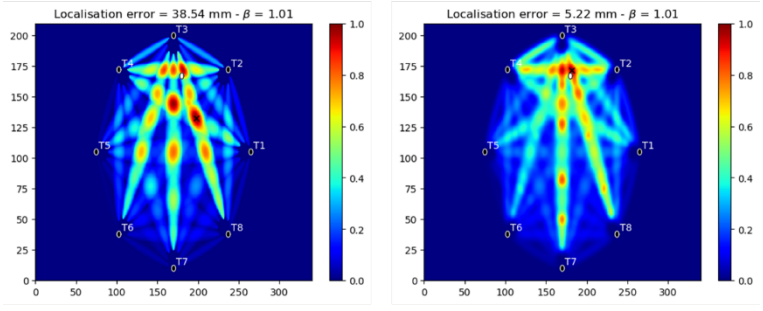

(d)

565

566 **Figure 14.** Tomographies for original RAPID (left) and E-RAPID (right) for simulations (a) P1S10, (b) P1S5, (c)
567 P2C10 and (d) P2C5 with constant $\boldsymbol{\alpha = 0.08}$ and $\boldsymbol{\beta = 1.01}$

568

569 As expected, a larger accuracy was achieved for the star configuration using the E-RAPID
570 algorithm (i.e., right side of Figure 14a and Figure 14b). It was observed that for this highly

irregular sensors array, the sharp improvement of the localisation error was observed both for the optimised and constant value of β. Consequently, the discussion made above also holds in case a constant β value is considered in the comparison, reinforcing the statement that the E-RAPID algorithm works satisfactorily for configurations with high unevenness of the sensing network density. Interesting results were also achieved for the case of the circular array. It should be reminded that a low value of β increases the tomography resolution, at the expense of the localisation precision. This can be clearly observed in the scenarios P2C10 and P2C5 for the original RAPID algorithm, where the high damage probability areas (i.e., red areas) in Figure 12 were reduced with respect to the areas in Figure 14. However, the probability ellipses did not completely cover the interrogated area. This drove the estimated maxima towards the areas with high intersections (refer to Figure 11), creating counter-intuitive results with an inaccurate localisation position. As observed for the cases P2C10 and P2C5 of the E-RAPID algorithm (Figure 14c and Figure 14d, right side), the averaging and filtering process reduced the false high probability in the highly intersected areas leaving a more intuitive conclusion, i.e., the estimated maxima was positioned on the pixels where the probability is high exclusively due to a high DI and not due to the inherent ellipses summation of the RAPID method. This aspect led to the conclusion that the selective use of E-RAPID may increase the localisation accuracy keeping a high resolution (i.e., a low value of β).

In conclusion, the proposed modifications to the RAPID algorithm satisfactorily improve the accuracy in the scenarios where the sensing network density presented inhomogeneity. As observed in Table 3, the minimum localisation error accuracy improvement was sharp for the star arrangements and moderate-to-high for the circular layouts. Also, the probability averaging and blur filtering processes allow reconstructing a smaller high damage probability area around the real damage position, as depicted in Figure 12.

4 Conclusions

A critical discussion of the advantages and flaws of the RAPID algorithm has been provided in the present work. Despite its easy implementation and wide-range use, the RAPID algorithm strongly depends on the disposition of the sensors and on the input parameters, e.g., on the value of the shape parameter β. A partial solution for the uneven sensing network density has been proposed and the performance evaluated using a dataset created from a layered-shell numerical model. The E-RAPID algorithm is based on two steps: (i) the unevenness of the tomography matrix is partially removed by an element-by-element normalization by the pixel-by-pixel intersection matrix and (ii) the tomography is smoothed employing a 2D Gaussian blur filter. The main conclusions drawn from the evaluation of the E-RAPID algorithm are:

- The localisation error of the E-RAPID algorithm diminishes with respect to the error from the original algorithm for the star and the circular sensor patterns. Quantitatively, the largest percentage of improvement (98.33%) is achieved with the star configuration for a through-hole of 10mm diameter and positioned at (x, y) = (114, 77)mm from the bottom left corner of the panel.
- The application of the proposed E-RAPID algorithm works better for layouts of sensors that show a highly non-homogenous sensing network density distribution.
- The averaging of the estimated probabilities by using the intersection matrix increases the resolution by reducing the dimensions of the high probability area around the damage. This was verified for the circular sensors arrangements considering the simulation with a 5mm diameter through-hole positioned in (x, y) = (180, 167)mm. This specific scenario was selected since the optimised β parameter was the same for the original and for the E-RAPID algorithms. The comparison showed that the E-RAPID algorithm provides a strong increase of the resolution along with a more accurate damage localisation estimation.

Declaration of competing interest

The authors declare that they have no known competing financial interests or personal relationships that could have appeared to influence the work reported in this paper.

Data Availability Statement

The raw/processed data required to reproduce these findings cannot be shared at this time due to technical or time limitations.

References

[1] IATA, "Airline Maintenance Cost: Executive Commentary Edition 2019 (FY2018 data)," 2019.

[2] F. G. Yuan, Ed., *Structural Health Monitoring (SHM) in Aerospace Structures*, 1st ed. Woodhead Publishing, 2016.

[3] Z. Su, L. Ye, and Y. Lu, "Guided Lamb waves for identification of damage in composite structures: A review," *J. Sound Vib.*, vol. 295, no. 3–5, pp. 753–780, 2006.

[4] L. Maio, V. Memmolo, F. Ricci, N. D. Boffa, E. Monaco, and R. Pecora, "Ultrasonic wave propagation in composite laminates by numerical simulation," *Compos. Struct.*, vol. 121, pp. 64–74, 2015.

[5] O. Putkis, R. P. Dalton, and A. J. Croxford, "The anisotropic propagation of ultrasonic guided waves in composite materials and implications for practical applications," *Ultrasonics*, vol. 65, pp. 390–399, 2016.

[6] S. Pant, J. Laliberte, M. Martinez, B. Rocha, and D. Ancrum, "Effects of composite lamina properties on fundamental Lamb wave mode dispersion characteristics," *Compos. Struct.*, vol. 124, pp. 236–252, 2015.

[7] B. Yang *et al.*, "Lamb wave-based structural health monitoring on composite bolted joints under tensile load," *Materials (Basel).*, vol. 10, no. 6, pp. 1–17, 2017.

[8] C. A. C. Leckey, K. R. Wheeler, V. N. Hafiychuk, H. Hafiychuk, and D. A. Timuçin, "Simulation of guided-wave ultrasound propagation in composite laminates: Benchmark comparisons of numerical codes and experiment," *Ultrasonics*, vol. 84, pp. 187–200, 2018.

[9] C. Sbarufatti, G. Manson, and K. Worden, "A numerically-enhanced machine learning approach to damage diagnosis using a Lamb wave sensing network," *J. Sound Vib.*, vol. 333, no. 19, pp. 4499–4525, 2014.

[10] C. Yang, L. Ye, Z. Su, and M. Bannister, "Some aspects of numerical simulation for Lamb wave propagation in composite laminates," *Compos. Struct.*, vol. 75, no. 1–4, pp. 267–

275, 2006.

[11] T. R. Hay, R. L. Royer, H. Gao, X. Zhao, and J. L. Rose, “A comparison of embedded sensor Lamb wave ultrasonic tomography approaches for material loss detection,” *Smart Mater. Struct.*, vol. 15, no. 4, pp. 946–951, 2006.

[12] X. Zhao, R. L. Royer, S. E. Owens, and J. L. Rose, “Ultrasonic Lamb wave tomography in structural health monitoring,” *Smart Mater. Struct.*, vol. 20, no. 10, 2011.

[13] X. Zhao *et al.*, “Active health monitoring of an aircraft wing with embedded piezoelectric sensor/actuator network: I. Defect detection, localization and growth monitoring,” *Smart Mater. Struct.*, vol. 16, no. 4, pp. 1208–1217, 2007.

[14] H. Sun, A. Zhang, Y. Wang, and X. Qing, “Baseline-free damage imaging for metal and composite plate-type structures based on similar paths,” *Int. J. Distrib. Sens. Networks*, vol. 15, no. 4, 2019.

[15] L. Qiu, B. Liu, S. Yuan, Z. Su, and Y. Ren, “A scanning spatial-wavenumber filter and PZT 2-D cruciform array based on-line damage imaging method of composite structure,” *Sensors Actuators, A Phys.*, vol. 248, pp. 62–72, 2016.

[16] K. Feng and Z. Li, “Damage imaging in composite laminates using phase reversal method,” *AIP Conf. Proc.*, vol. 2102, no. May, 2019.

[17] A. Ebrahimkhanlou, B. Dubuc, and S. Salamone, “Damage localization in metallic plate structures using edge-reflected lamb waves,” *Smart Mater. Struct.*, vol. 25, no. 8, pp. 1–13, 2016.

[18] Z. Liu, X. Zhong, T. Dong, C. He, and B. Wu, “Delamination detection in composite plates by synthesizing time-reversed Lamb waves and a modified damage imaging algorithm based on RAPID,” *Struct. Control Heal. Monit.*, vol. 24, no. 5, pp. 1–17, 2017.

[19] G. Azuara, E. Barrera, M. Ruiz, and D. Bekas, “Damage Detection and Characterization in Composites Using a Geometric Modification of the RAPID Algorithm,” vol. 20, no. 4, pp. 2084–2093, 2020.

[20] N. MECHBAL and M. REBILLAT, “Damage Indexes comparison for the structural health monitoring of a stiffened composite plate,” in *VIII ECCOMAS Thematic Conference on Smart Structures and Materials SMART*, 2017.

[21] M. Moix Bonet, B. Eckstein, R. Loendersloot, and P. Wierach, “Identification of Barely Visible Impact Damages on a Stiffened Composite Panel with a Probability-based Approach,” in *DEStech Publications*, 2015.

[22] M. Voß *et al.*, “Numerical simulation of the propagation of Lamb waves and their interaction with defects in C-FRP laminates for non-destructive testing,” *Adv. Compos. Mater.*, vol. 29, no. 5, pp. 423–441, 2020.

[23] P. Deng, O. Saito, Y. Okabe, and H. Soejima, “Simplified modeling method of impact damage for numerical simulation of Lamb wave propagation in quasi-isotropic composite structures,” *Compos. Struct.*, vol. 243, no. January, p. 112150, 2020.

[24] A. De Luca, F. Caputo, Z. Sharif Khodaei, and M. H. Aliabadi, “Damage characterization of composite plates under low velocity impact using ultrasonic guided waves,” *Compos. Part B Eng.*, vol. 138, no. August 2017, pp. 168–180, 2018.

[25] A. Huber, “No Title.” [Online]. Available: https://www.dlr.de/zlp/en/desktopdefault.aspx/tabid-14332/24874_read-61142/.